Forward modelling on GPR responses of subsurface air voids

Tess X.H. Luo[1], Wallace W.L. Lai[1*], Antonios Giannopoulos[2]

[1].Department of Land Surveying and Geo-informatics, The Hong Kong Polytechnic University, Hong Kong
[2].School of Engineering, University of Edinburgh, Edinburgh, United Kingdom
* Corresponding author: ZS615, The Hong Kong Polytechnic University, Hung Hom, Hong Kong. email: wllai@polyu.edu.hk

Abstract Along with the development of urbanization, an increasing number of subsurface voids in urban cities can have serious effects on the expected functionality of key infrastructure elements such are roads. Ground penetrating radar is an effective technique for imaging the subsurface and detect such air voids. The GPR responses of air voids with different horizontal width were quantitively investigated in this study using forward modelling: empirical experiments in both laboratory and site; as well as numerical simulations with FDTD. Two typical road constructions were modelled: reinforced concrete pavements and bituminous pavements, where the majority of underground utility networks are buried underneath. Pulse GPR signals having two centre frequencies: 600MHz and 200MHz were simulated. It was observed that the ratio of void size and GPR signal wavelength would result in various patterns in the GPR B-scans: they can be a hyperbola, a cross pattern, a bowl shape pattern, and a plain reverberation pattern. And GPR responses of voids under road structures were distorted by reinforcement and interface of road layers. With signatures of air voids appeared in GPR B-scans through validation by lab experiments and ground truthung, confidence of void identification will be enhanced.

Keywords Ground Penetrating Radar, subsurface air void, forward modelling, FDTD simulation

1. Introduction

In metropolises like Hong Kong and elsewhere, there are multiple facilities buried underneath the road; they are, for example, power, water, drainage, sewerage, lighting or communication and so on (Farley et al., 2001; Lai et al., 2017; Lai et al., 2016). Subsurface water pipe leakage causes underground wash-out, leaving an air void when water is drained and finally resulting in road collapse when the damaged area can no longer support the heavy load of the pavement structure and its traffic. Over time, countless numbers of air voids develop beneath a city's road network, which threatens the safety of the life and property of citizens.

Ground penetrating radar (GPR) is a non-destructive technique that use electromagnetic (EM) waves to image the near subsurface. It has been proved effective and efficient in detecting the properties change. However, GPR responses are affected by multiple factors, including dielectric contrast between materials, background scattering, the geometry of reflectors. Therefore, subsurface voids can yield different GPR responses depending on the size and their surroundings. Interpretation of GPR data can be biased and costly in terms of data collection and interpretation, in which; established knowledge base and experiences are required before a judgment can be made. An illustration is a GPR survey conducted by Lai et al. (2018), in which the human interpretation

41 of GPR data of a 100 m^2 site took a week and ended up an accuracy of approximately 78% accuracy.
42 Thus a more effective method is in need to improve the efficiency of subsurface void detection
43 with GPR. If preliminary knowledge on how voids could look like in a GPR B-scans is readily
44 available, potential voids could firstly be described and located with automatic techniques, and
45 then confirmed with human intervention, instead of the ineffective human interpretation described
46 in (Lai et al., 2018). This study aims at presenting an initial attempt to quantify GPR responses of
47 voids using forward modelling for constructing the voids' GPR signatures. Two aspects were taken
48 into consideration in this study, they were standard road designs, and air void geometry.

49 2. GPR response of voids

50 2.1 Theoretical background

51 GPR imaging is based upon the propagation, reflection and measurement of EM waves (Annan,
52 2004; Jol, 2009). When the EM wave encounters any electrical parameter contrast in the ground,
53 it is backscattered and received by the receiving antenna. The main electrical parameters of any
54 medium, i.e. the permittivity, the permeability and the conductivity, are generally a function of
55 frequency. B-scans and C-scans are two forms of GPR data presentation from 2 to 3 dimensions.
56 B-scans describe the vertical section of the subsurface world along the survey traverse. A C-scan
57 is formed by stacking multiple B-scans collected in this horizontal plane, and then plotting the
58 amplitudes of the recorded data at a given time (Goodman & Piro, 2013).

59 Each urban subsurface defect may yield specific GPR responses. GPR responses are affected by
60 multiple factors: electromagnetic properties of the host material and the geometric of the object
61 as a reflector. In practice, the GPR reflections from one kind of object are never the same, as the
62 real underground world is very complicated. Therefore, GPR responses of each urban defects are
63 needed to be standardized and quantified.

64 Air voids are one of the most threatening subsurface defects in urban areas. The strong permittivity
65 contrast between the soil surrounding the void and the air in the void leads to localized GPR
66 reflections stronger than the background. Many researches have investigated GPR responses of
67 voids. Xu et al. (2010) used GPR to detect several common subsurface voids, and found that
68 narrow cracks in the infrastructure yield hyperbola responses. Lai et al. (2017) concluded that
69 voids would ragenerate reverberate-like GPR responses. Casas et al. (1996) illustrated that if the
70 void was much smaller than the GPR wavelength, diffracting hyperbolas occur in GPR B-scans.
71 On the contrary, if voids' diameters are much larger than the wavelength, irregular signals with
72 chaotic reflections and a decrease of the received frequency. Kofman et al. (2006) simulated GPR
73 responses with GPRMax and indicated that oscillations happened only when the void size was
74 significantly larger than the GPR wavelength. It was believed that the strong reflections with
75 reduced frequency – the reverberation response – were caused by air voids (Kofman et al., 2006).
76 All these researches demonstrated that air voids generate special GPR reflections – hyperbola or
77 reverberation, and the ratio of the void size to the GPR wavelength yields a significant impact on
78 GPR responses. However, there is little reference based on rigorous basis for quantifying the
79 relationship between (1) the GPR wavelength controlled by the instrumentation and (2) physical
80 size of air voids.

2.2 Theoretical background on the numerical simulation

2.2.1 Finite difference time domain (FDTD) modelling on GPR

Controlled environments in the subsurface are difficult to be constructed in real-world, and ground-truthing is not always possible. The numerical simulation is another effective way to model the desired situation. Currently, there are many numerical simulation methods that can be used to model electromagnetic wave, among which method of motion (MoM), finite element method (FEM) and finite difference method (FDTD) are the most widely used methods (Davidson, 2010). The FDTD is more suitable for modelling GPR wave because it is based on Maxwell's equations and it allows the user to specify the material at all points within the computational domain (Davidson, 2010).

The FDTD algorithm was first proposed by Yee (1966), who employed second-order central differences. The algorithm replaces all the derivatives in Ampere's and Faraday's laws with finite differences. It discretizes space and time so that the electric and magnetic fields are staggered in both space and time (Schneider, 2010). Then by solving the resulting differential equation, the "update equations" that denote the unknown future fields are obtained from the known past fields (Warren et al., 2016).

Therefore, the future electric field can be updated from past magnetic fields, and vice versa. Imagine there is a one-dimensional space where both E (electric field) and H (magnetic field) exist. The time-domain space is discretized by a space step Δx and a time step Δt, as illustrated in Figure 1.
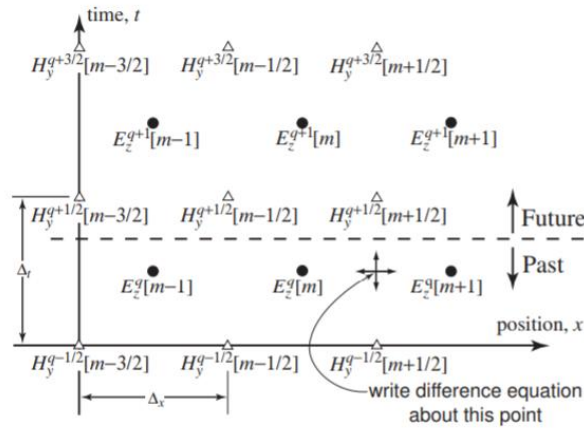

Figure 1 Illustration of one-dimensional EM field in FDTD modelling (Schneider, 2010). The index m corresponds to the spatial step, effectively the spatial location, while the index q corresponds to the temporal step. E is the electric field, and H is the magnetic field.

With Δx and Δt describing the spatial step in E and H, at the specific position $\left(\left(m + \frac{1}{2}\right)\Delta x, q\Delta t\right)$, where the black arrow points to in Figure 1, equation [1-2] is obtained.

$$H_y^{q+\frac{1}{2}}\left[m + \frac{1}{2}\right] = H_y^{q-\frac{1}{2}}\left[m - \frac{1}{2}\right] + \frac{\Delta t}{\mu\Delta x}\left(E_z^q[m + 1] - E_z^q[m]\right) \qquad [1]$$

$$E_z^q[m + 1] = E_z^q[m] + \frac{\Delta t}{\epsilon\Delta x}\left(H_y^{q+\frac{1}{2}}\left[m + \frac{1}{2}\right] - H_y^{q+\frac{1}{2}}\left[m - \frac{1}{2}\right]\right) \qquad [2]$$

107 The FDTD method can be expanded to multi-dimensions. In terms of a single spatial dimension
108 where the electric and magnetic fields are offset a half spatial step from each other. Equation [1-
109 2] shows that electromagnetic properties of the host material, and the spatial step, determine the
110 simulated signals. In this study, numerical simulations were conducted with GPRMax, an open-
111 source FDTD simulation package that allows users to simulate the GPR response to the subsurface
112 world (Giannopoulos, 2005; Warren et al., 2016).

113 When performing the FDTD simulation, the number of iterations determines the FDTD resolution
114 of a given time window. It can be observed from the above equations that the step sizes in 3D –
115 Δx, Δy, Δz and Δt – are correlative with each other. To ensure that the simulation runs stably, the
116 CFL condition (as per Equation 3) has to be met (Courant et al., 1928):

$$\Delta t \leq \frac{1}{c\sqrt{\frac{1}{(\Delta x)^2} + \frac{1}{(\Delta y)^2} + \frac{1}{(\Delta z)^2}}} \qquad [3]$$

117 where c is the speed of light, hence Δt is constrained by the values of Δx, Δy and Δz.

118 A rule-of-thumb is that the discretization step should be at least ten times smaller than the smallest
119 wavelength of the propagating electromagnetic fields; otherwise unexpected dispersion may occur.
120 Other factors, such as energy sources, field boundaries, and lossy materials have been well
121 discussed in the literature (Hastings et al., 1995; Hastings et al., 1996; Schneider, 2010; Warren et
122 al., 2016; Yee, 1966). The four important material properties: relative permittivity, conductivity,
123 relative permeability, and magnetic loss should be defined clearly in the forward simulation.

2.2.1 The complex refractive index model (CRIM)
125 The permittivity and conductivity of some widely seen materials are defined in ("ASTM D6432,"
126 2011). The subsurface world is very inhomogeneous and different layers may compose of various
127 aggregate sizes. Therefore the porosity of each layer is different, and percentages of air or water
128 within the layer change accordingly, but the discrepancies shall not be significant. The complex
129 refractive index model (CRIM) was applied to determine the permittivity of each material in this
130 study. The CRIM as in equation [4], which take the air and water content into consideration, is
131 proved reliable in higher frequency (around 1GHz) (Chan & Knight, 2001; Lai et al., 2006).

$$\sqrt{\varepsilon'_c} = S_w \phi \sqrt{\varepsilon'_w} + (1 - S_w)\phi\sqrt{\varepsilon'_a} + (1 - \phi)\sqrt{\varepsilon'_s} \qquad [4]$$

132 where ε'_c, ε'_w, ε'_a and ε'_s are real permittivity of the composite, water, air and soil particle,
133 respectively. S_w is the degree of water saturation and ϕ is the porosity.

2.3 Standard road structure
135 In order to model the situation of the voids under roads, the structure of roads must be coherent
136 with reality. Bituminous road and reinforced concrete paved roads are two most commonly seen
137 pavement structure in Hong Kong. Highway department of Hong Kong establishes guidelines on
138 typical road pavement constructions, as shown in Figure 2 *(HyD, 2017a, 2017b)*.
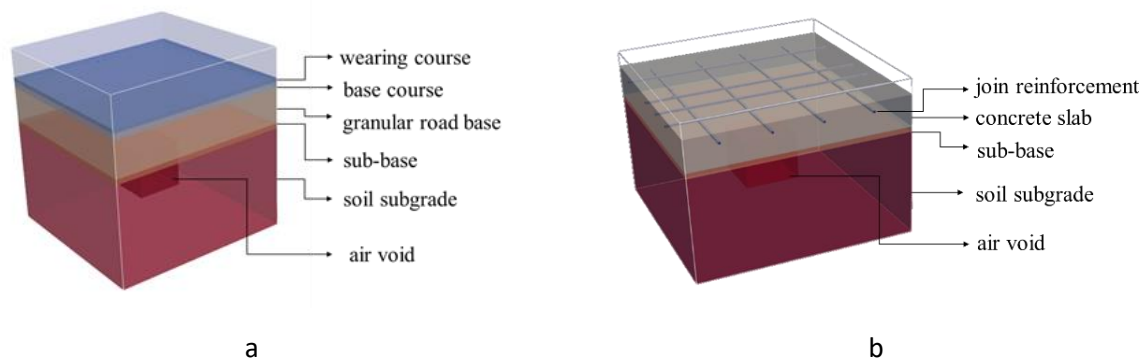
Figure 2 Simulation model of two typical road structures: (a) is a bituminous road model, and (b) is a concrete road model

The structure of the bituminous pavements is relative homogeneous. Typical bituminous pavements consist of five layers: 0.04m thick wearing course, 0.065m thick base course, approximately 0.4m thick granular road base, and sub-base and soil subgrade. The above three layers are constructed by bitumen but with aggregates in different sizes: aggregate size increases along with vertical depth, ranging from 0.02m to 0.04m. Large aggregate sizes may lead to higher porosity and more blank space among aggregates.

There are standards that suggest the ranges of several typical materials ("ASTM D6432," 2011; UUS-SPEC, 2019). The CRIM was applied to estimate the relative permittivity of each layer with the size of aggregate considered. In the CRIM estimation, portions of air and water dominate the material's permittivity, but blank space and water are in relatively insignificant in the compacted roads with standard 5% void ratio, therefore the variation of the permittivity among road layers were not significant.

In terms of the concrete roads, usually a concrete pavement consists of three layers: 0.3m thick concrete slab where mesh reinforcements are integrated, 0.05m thick sub-base filled by the granular material or lean concrete, and subgrade with soils. The maximum spacing of the joint reinforcement is 0.3*0.45m in longitude and latitude, respectively, with a top cover appropriately 0.06m thick. Air voids are usually found in the subgrade layer where most underground unities are buried in. Because the joint-mesh reinforcement would generate strong resonance in the GPR survey, distortions on GPR response of voids in subgrade are expected.

The variations of the permittivity of the concrete and the metal are both not significant. Therefore the built-in example of the permittivity of the metals in GPRMax was applied to model the reinforcement in the concrete road models. The relative permittivity of the concrete slab in the concrete road model was adopted from the reference in ASTM ("ASTM D6432," 2011).

It is hard to measure the electromagnetic properties from real sites because the ground truthing is not always desirable. The conductivity and permeability of each road layers were adopted from literature ("ASTM D6432," 2011; Cullity & Graham, 2008; NDT.net, 2011). In addition, although air voids are more likely to be irregular, our model assumes rectangular voids for efficiency of building model and computation on the basis that reality is still adequately presented. Table 1 presents the parameters used in the FDTD simulation

170　　　　　　　　　　　　　Table 1Parameters of the road models with the FDTD simulation

	Layer	Permittivity	Conductivity	Permeability	magnetic loss	Step size
Bituminous road	Wearing course	8	0.05	1	0	0.006
	Base course	9	0.08	1	0	
	Road base	9	0.01	1	0	
	Sub-base	10	0.01	1	0	
	Soil subgrade	9	0.02	1	0	
Concrete road	Concrete slab	6	0.001	1	0	0.006
	Sub-base	9	0.1	1	0	
	Soil subgrade	9	0.2	1	0	

171

172　2.4 Forward modelling on GPR responses of voids in laboratory

173　To study how voids in the relative homogenous environment are presented in GPR data, subsurface
174　voids with varying horizontal spread were created in the Underground Utility laboratory of the
175　Hong Kong Polytechnic University (PolyU) (Wu, 2015). The tank was filled with soil. GPR
176　profiles were collected with an IDS 600MHz system and processed according to the typical process
177　flow proposed by Jol (2009) (in 2D) and Luo et al. (2019) (in 3D). Numerical simulations that
178　imitated the laboratory experiment were conducted with GPRMax (Luo & Lai, 2020). In the
179　simulation models, voids with varying horizontal and vertical size were placed at shallow depth
180　(0.1m) within a soil environment – a relatively homogenous environment. Simulated signals were
181　transmitted and received by a 900MHz common offset antenna unit with 0.15m antenna offset.
182　The EM parameters of the FDTD model of the laboratory were estimated by the inverse study with
183　the laboratory data. The relative permittivity of the model was estimated as 11 with the wave
184　velocity (0.09m/ns) of the laboratory data with Equation [5]. The electrical conductivity and the
185　magnetic permeability of the model were adopted from the built-in example of the software
186　GPRMax. The step size of the simulations was 0.006 – meet the CFL condition (as equation [3]).
187　In addition, a surface roughness (±5mm) was randomly placed on the boundaries of voids as an
188　assumption of roughness across the soil and air interface, making the backscatter field from the
189　modelled voids more realistic..

$$v = \frac{c}{\sqrt{K}}$$　　　　　　　　　[5]

190　where c is the wave velocity in free space, which is approximately 0.2998m/ns; v is measured
191　velocity, and K is the relative permittivity.

192　The laboratory experiments and simulations produced similar GPR responses. Three typical void
193　patterns were identified in the B-scan –cross, bowl shape, and plain reverberation - and these
194　patterns appeared in succession as the void's spread grew, as can be seen in the 5[tt]-6th rows in
195　Table 2.

196　Table 2 Forward modelling of surface voids with different horizontal spreads in the laboratory (Luo &
197　　　　　　　　　　　　　　　　　Lai, 2020; Wu, 2015)

Void spread (VS)	0.4m	0.6m	0.75m	0.1m	1.25m

Simulation model					
FFZ (900MHz)	0.09m				
Ratio of VS-FFZ	4	6	8	10	12
FDTD simulation (B-scan)					
Laboratory experiment (B-scan)					
Laboratory experiment (C-scan)					
Pattern	cross	cross	bowl	bowl	plain reverbration

198 Remark: the size of B-scans in 5th and 6th rows are 2m length and 0.7m deep; C-scans in
199 7th row present the survey area that was 2m *1.5m large.

200 It is noticeable in Table 2, that in parallel with the increase of void horizontal spread, the
201 hyperbolic reflections from the void's edges also become more widely separated. When tw o
202 hyperbolas overlap, cross patterns occur. Whether two signals can be distinguished, depends on
203 GPR spatial resolution, while GPR horizontal resolution is determined by the footprint of a GPR
204 beam. A narrower beamwidth with a smaller footprint provides a better spatial resolution. The
205 GPR horizontal resolution was calculated after making use of a simplified model (Equation [6])
206 developed by Annan & Cosway (1992),. It determines the GPR footprint with the First Fresnel
207 Zone (FFZ)..

$$\mathrm{r}(v,z,f) = \sqrt{\left(\frac{v^2}{16f^2} + \frac{vz}{2f}\right)} \qquad [6]$$

208 Where r is the radius of FFZ, z denotes depth, f is the standard for dominant frequency, and
209 v is GPR wave velocity.

210 Because the footprint is dominated by wavelength and depth, and the void pattern is wavelength
211 dependent, the footprint is calculated as 0.09m to eliminate the influence of void depth. It is
212 observed that when the void spread is about5 times than $\mathrm{r}(v,z,f)$ in Equation [6], the GPR

213 reflection appears as a cross. A bowl shape pattern presents when the void spread is larger than 8
214 times of r(v, z, f). When the void spread is far larger than GPR footprint, reflections of two edges
215 of voids become entirely separated, and a plain plateau with reverberation is bounded between the
216 two edges. This kind of pattern is named plain reverberation in this study. Therefore, the ratio of
217 void size to GPR footprint determine the pattern of GPR reflections, which must be well taken
218 care of in void detection by GPR. While on plan represented by C-scans in the 7th row, voids are
219 always present as local reflections with high intensity, though they are different in sizes but the
220 differences in B-scan patterns do not apply.

221 However, discrepancies between the simulated B-scans and collected data were observed. The
222 void tops – the upper boundary between the air and the soil – are clearly shown in the simulated
223 B-scan (5th row), but are invisible in the laboratory B-scans (6th row). In the numerical modelling,
224 the effects of the surrounding material were eliminated by subtracting the signal of the surrounding
225 material, as shown in Equation [7]. The patterns shown in the 5th row of Table 2 present the GPR
226 reflection generated by air-voids only. It includes the reflection from the upper air-soil boundary.
227 On the contrary, in the laboratory experiments, air voids were dug from the surface of the soils.
228 The phase of the upper boundaries of voids was overlapped with the phase of ground wave. There
229 are two reasons of the discrepancies. Firstly, the time-vary gain and the background removal, were
230 applied to the laboratory data, as a result, the reflections of the void tops were removed. Secondly,
231 Mie type scattering in the laboratory B-scans contributes to the collected B-scans but not FDTD
232 simulations. These two reasons lay the uncertainties of the forward models and the extent of these
233 uncertainties can vary from one field site to another.

$$\begin{aligned}reflection\ of\ voids \\ = signal\ of\ model\ with\ void \\ - signal\ of\ model\ without\ void\end{aligned} \qquad [7]$$

234

3. Forward modelling on GPR responses of air voids under road subsurface

237 Ground collapses usually happen on road surface: busy roads are always suffering from heavy
238 loading, and if there are large air voids beneath, the road structure hardly survives. However, in
239 the real world, the subsurface world is not as homogeneous as that of the laboratory and previous
240 models. Hence it is impossible to have regular and straightforward void patterns as the ones
241 presented in Table 2. Hence further simulation based on a real road structure is presented in
242 following section.

3.1 A site experiment on void under road structure

244 A site experiment was conducted on Shek Mun, Hong Kong, to investigate how air voids present
245 themselves in GPR representation (B-scans and C-scans) (Lai et al. 2018). As shown in Figure
246 3(a), the survey site consists of two parts: a section of concrete paved road and another section of
247 block paved road. In total, six fit balls with various spread were buried at different depths beneath
248 the road sections (Figure 3.b). There are two utilities located across the survey site: a PVC pipe (ø:
249 0.1m) and a ductile iron (D.I) pipe, (ø: 0.2m), for observing their interference on the signals of the
250 voids..

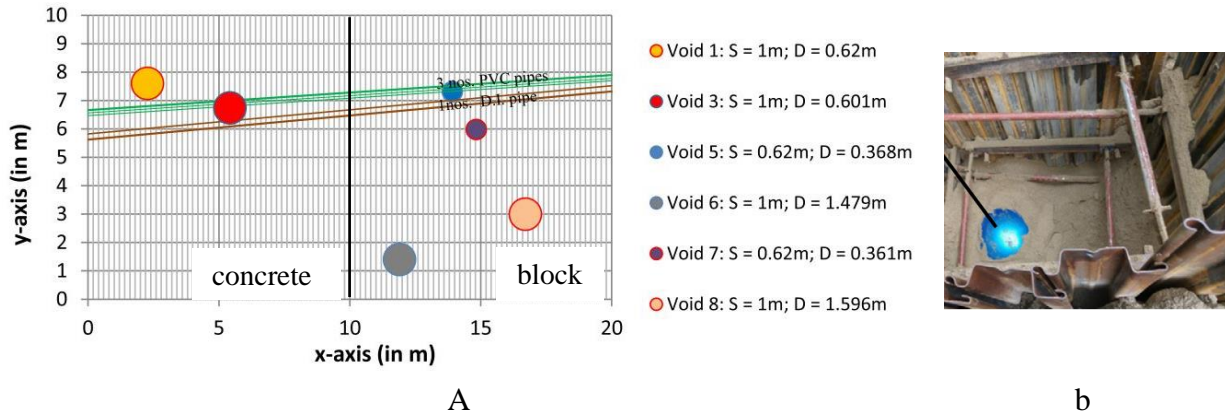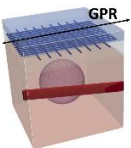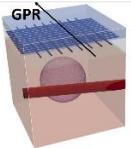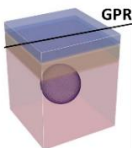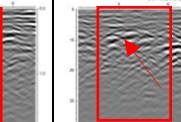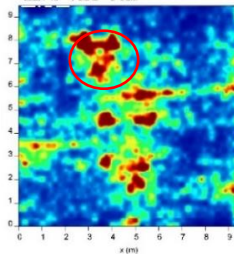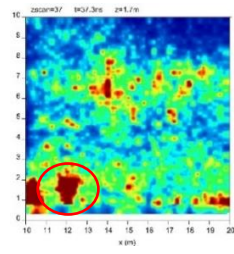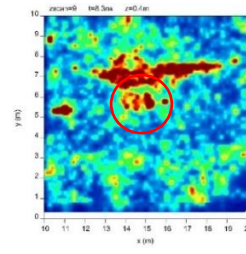A   b
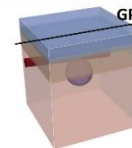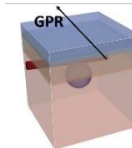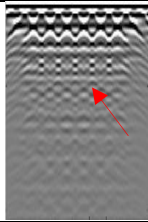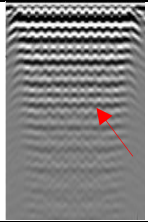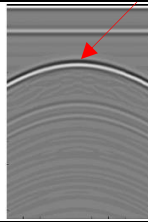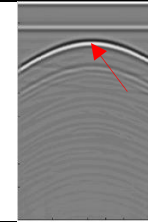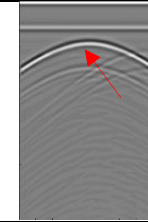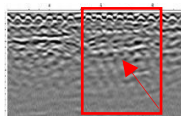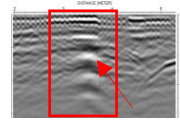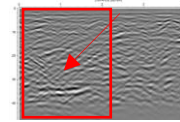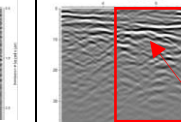
Figure 3 Illustration of the site and buried balloons in Shek Mun: (a) is the concept drawing of the site, while (b) is a photo of the buried fit ball.

GPR B-scans were collected by a dual-frequency (600/200 MHz) IDS model, following an orthogonal grid with a 0.25m profile spacing. GPR B-scans were processed according to Jol (2009) and Luo et al. (2019) to generate C-scans. Three representative fit balls were selected for further analysis: void 1, void 6 and void 7 with reference to Lai et al. 2018. Specifically, void 1 was buried under the mesh rebar, void 7 was close to the D.I pipe, and Void 6 was buried deeper (1.479m). The spacing of the mesh rebar in the concrete paved road section was 0.1m. Considering the subsurface void is often caused by pipe leakage, the effect from the utility nearby on the detection of voids could also be observed.

The underground environment was inhomogeneous and complex at the site, because the survey area was backfilled with the excavated soil, which resulted in heavy scattering compared with the laboratory case (Lai et al., 2018). FDTD simulations were also carried out to model the GPR B-scans of the voids that are free from any other scattering, apart from road structure and utilities. Simulated models were designed base on the fit balls buried in the site. The electromagnetic properties of each road layers utilized the values in Table 1, and the step size was 0.006 – same as the laboratory experiment. GPR data of 600MHz was applied in this study for the sake of better resolution. Basic signal processing, like filters and gains, were applied on B-scans. The B-scans and C-scans are displayed in Table 3.

Table 3 Forward modelling on air voids with different horizontal spreads in the site

Balloon	Void 1		Void 6	Void 7	
Simulation Model					
FFZ (600MHz)	0.24 m		0.37m	0.19m	
Ratio of VS-FFZ	4.2		3	3	

FDTD simulation (B-scan)				
Site experiment (B-scan)				
Site experiment (C-scan)			
Pattern	resonance	Hyperbola	hyperbola

271   Remarks: The dimension of the FDTD simulations in the 5th row are the same as the red
272   rectangles in the corresponding 6th row: 1.5m long * 1.5m deep. The C-scans in the 7th row
273   present the survey area that was 9m*9m large. Red arrows point to the location of voids.

274 Table 3 is divided into three parts according to void spreads. Part 1 (the 2nd to 5th row) illustrates
275 the simulation models and simulated GPR B-scans via the calculated FFZ. Part 2 experiments (the
276 6th to 7th row) presents the B-scans and C-scans of the site experiment. Part 3 pattern interpretation
277 (the last row) suggests the type of void patterns. The fit balls appears as regular spheres, while the
278 flattened hyperbolic patterns were expected in the B-scans. B-scans of Void 1, both experimental
279 and simulated B-scans, show that the GPR responses were broken into sections by tails of rebar
280 reflections. Besides, it can be observed from both simulated and experimental B-scans that the
281 resonance of GPR responses from void 1 were more obvious than that of the other two voids. The
282 resonant GPR response generated by voids under the reinforcement last through longer time/depth
283 – coincide with the observation in Table 3 and Lai et al. (2017): that the resonance of GPR
284 reflection of voids decay in the time window. The GPR responses of void 7 presented as flatten
285 hyperbola in both the experimental and simulated B-scans. The interference from the nearby utility
286 was clearly visible in the experimental and simulated B-scans. However, the simulated GPR
287 responses of void 6 located shallower than that in the experimental B-scans. It was possible that
288 the buried depth of the fit ball 6 (void 6) may move in reality after backfillof the upper soils. In
289 contrast to the void 1 in concrete paved road, the resonance of GPR reflections were not visible in
290 the B-scans of void 6 and void 7 in the bitumen paved road. In terms of C-scans in the 7th row, all
291 three voids appear as local and high reflections, which is coherent to the result of the laboratory
292 experiment.

293 Besides, the simulation and experiment agreed that the interferences of the road layers were not
294 significant in both experimental and simulated B-scans. Specifically, void 6 and void 7 appear as
295 a continuous and plain pattern. However, in many cases, flat subsurface layers and utilities parallel
296 to the GPR traverse also generate plain GPR reflections. The means to distinguish voids with large

297 spread and utilities is to observe the horizontal length of plain pattern generated by voids is
298 restricted by the spread of voidswhich are much shorter in general.

299 Similar to the reasoning of discrepancies between simulated and experimental B-scans in Table 2,
300 the experiment data (B-scans in 6th row and C-scans in 7th) suffer heavy scattering. Mie type
301 scattering, which caused by the reflector's size similar to the GPR wavelength, happened in the
302 complicated and inhomogeneous subsurface world which contribute to the said discrepancies.
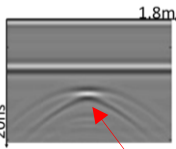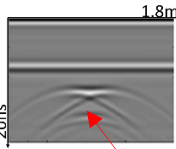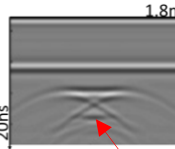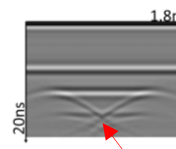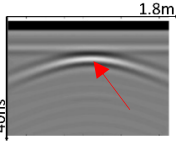
303 3.2 FDTD simulations of GPR responses of voids under roads
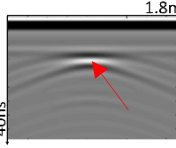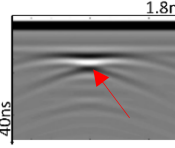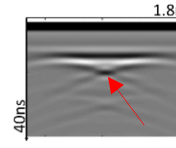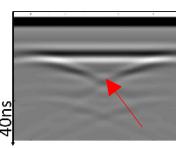
304 The observations of lab experiment and lab simulation are in agreement about the effects of void
305 size on the GPR reflections, while those of the Shek Mun site experiment and the simulation are
306 in line on the effect of the road structure on the GPR reflections. Unfortunately, it is not feasible
307 to dig or bury a number of voids under the road structure in practice, then FDTD simulation can
308 be used to study the combined effect of the void size and the road structure. Based on the typical
309 road structures, GPR B-scans of air voids with difference spreads and depths were modelled with
310 the FDTD simulation. The void embedded in models varies in the horizontal spread – range from
311 0.2m to 1.8m – while maintaining the 0.5m vertical size.

312 3.2.1 GPR response simulations on voids under bituminous roads

313 The FDTD simulated GPR reflections of voids under a bituminous road were similar to that of the
314 laboratory environment: similar patterns with particular shapes were presented. The aggregate
315 clusters generate scatterings, but they were not as strong as that of the air void, as shown in Table
316 4.

317 Table 4 Forward modelling of air voids with different horizontal spreads in the bituminous road
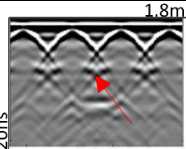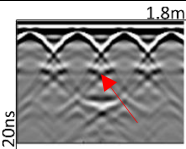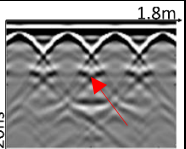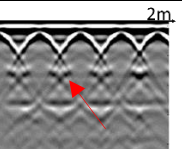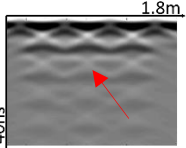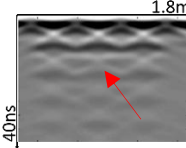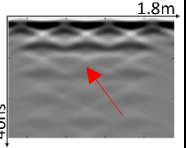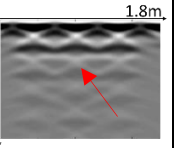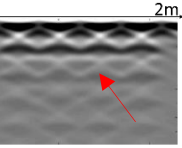
Void spread	0.3m	0.5m	0.8m	1.2m	1.8m
FFZ (600MHz)	0.24m				
Ratio of VS-FFZ	1	2	3	5	8
600MHz					
Pattern (600MHz)	hyperbola	cross	Cross	bowl	bowl
FFZ (200MHz)	0.51m				
Ratio of VS-FFZ	1	1	1	2	4
200MHz					
Pattern (200MHz)	hyperbola	hyperbola	hyperbola	cross	cross

318   The calculated radar footprint, in this case, were 0.24m and 0.51m for the 600MHz and 200MHz
319   antenna respectively. These footprints are significantly larger than that of the shallow void
320   experiments conducted in the laboratory. According to the laboratory results based on the shallow
321   voids, a shallow void with spread larger than 0.8m would generate a plain reverberation pattern if
322   the 600MHz signal was applied. But in the bituminous road simulation, the same 0.8m large void
323   generated a cross pattern responses. The vertical location - depth - of voids were different in these
324   two simulations. Thus the GPR footprints, which increase along with the penetrating depth, in two
325   simulations were different. Therefore, it was proven that the GPR responses were related to the
326   ratio of the GPR footprint to the void spread. When the 600MHz signal was applied, a cross shape
327   pattern is expected if the void spread was between 0.4m to 1m, and the simulation results were
328   coherent with this hypothesis. Voids with 1.2m and 1.8m horizontal spread generated bowl shape
329   responses in the 600MHz B-scans. It is consistent with a laboratory experiment that: when the void
330   spread is around 6 times larger than the GPR footprint, a bowl shape pattern was generated.

331   ### 3.2.2   GPR response simulations on voids under concrete roads

332   The simulations of the GPR response of air voids under the concrete pavements are displayed in
333   Table 5. Apparently, the GPR reflection of voids was significantly distorted by concrete rebar on
334   top of it, which is coherent with that of the Shek Mun experiment and simulation in Table 3. The
335   reflections from the rebar interfere with the reflection from the edge of air void beneath. In B-
336   scans of 600MHz, the GPR reflections of the top of the void, which ispresented as the middle of
337   the GPR pattern, were delayed to a lower time/depth. Then the pattern of the void was more like
338   the bowl shape pattern: closer to time zero at the edges and farther away from time zero in the
339   middle.

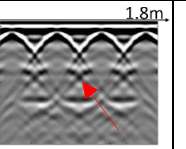340   Table 5 Forward modelling on air voids with different horizontal spreads in the concrete road
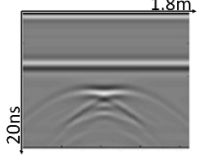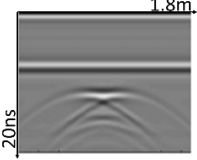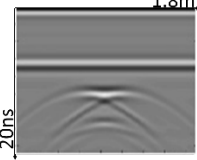
Void spread	0.3m	0.5m	0.8m	1.2m	1.8m
FFZ (600MHz)	0.20m				
Ratio of VS-FFZ	1	2	4	6	9
600MHz					
Pattern (600MHz)	hyperbola	cross	Cross	resonance	resonance
FFZ (200MHz)	0.44m				
Ratio of VS-FFZ	1	1	2	3	4
200MHz					
Pattern (200MHz)	resonance				

341 As the void spread increases, GPR reflections of void edges keep separating. But the interference
342 with the rebar responses was too strong that interfere the edge reflections of the voids, such that
343 the shape of the void responses were seriously distorted compared to the pattern in the modelling
344 of bituminous roads. Although the cross shape and bottom shape patterns were still distinguishable,
345 they were not as clear as that presented in Table 2 and Table 4. This obervation accords with the
346 relationship between GPR footprints and void spread. Also as shown in the B-scans of 600MHz,
347 when the void spread was larger than the spacing of the reinforced rebars, the void reflections
348 become discontinuous, and the original flat shapes as expected in the modelling of bituminous
349 roads are no longer distinguishable. On the other hand, the reverberations of the GPR reflections
350 in the larger depth were much more significant than that in the bituminous road. It also coincide
351 with the observation of the Shek Mun site experiment reported in Table 3.

352 3.2.3 GPR response simulations on voids with various thickness

353 'How thick is the void?' is an usual question for void detection. To further investigate whether
354 voids with various thicknesses would generate a different response in the GPR survey, forward
355 simulations were conducted on the bituminous road model, because the host materials in the
356 bitumen road were relatively homogenous. The horizontal void spread was maintained as 0.5m,
357 and the vertical size of voids was changed from 0.3m to 0.5m. The simulated B-scans are displayed
358 in Table 6.

359 Table 6 Forward modelling on air voids with different vertical size in the bituminous road

Void Vertical Size	0.3m	0.4m	0.5m
600MHz			
Pattern (600MHz)	cross	Cross	cross

360 **4.** The discrepancy among the GPR responses of voids with different vertical sizes was not
361 apparent. The three simulations in Table 6 all showed a cross-shape pattern. But it was
362 visible that, along with the increase of the thickness, the distance between the reflection of
363 the void top and that of the void bottom increased as well. At a depth of the void top, the
364 radar footprint was smaller and yielded a cross pattern. Then, at void bottom, radar
365 footprint was larger than the responses of two void edges which cannot be separated and
366 thus, result in a hyperbola pattern. These observations are very similar to the reverberation
367 patterns reported in the above sections. Distinction between the effects of vertical void size
368 and reverberation seems not feasible. Therefore, we don't suggest to estimate vertical void
369 size according to GPR B-scans.**Discussion**

370 The forward modelling from both experiments and FDTD simulations illustrated that subsurface
371 air voids would generate specific GPR responses. The factors that determine how GPR responses
372 look like were quantified.

373 4.1 Two characteristics

374 1) Horizontal spreads of voids determine the patterns of GPR responses

375 Comparing the three simulations – in-laboratory, in-site, and modelled roads, it can be concluded
376 that when the void spread along GPR traverse is very small, for instance, less than the radar
377 footprint; the hyperbola shape reflection is generated because of the air void acting similar to a
378 point reflector. When the void spread increases to 4-6 times the GPR footprint, the GPR response
379 of the air void appears as a cross shape pattern, because the reflection of two edges of the air void
380 is neither coincided nor totally separated. As the void spread increases to more than 6-8 times of
381 the radar footprint, the reflection of two void edges are completely separated, and the middle of
382 the void gradually shows up, so a bowl shape pattern appears. If the void spread along the GPR
383 traverse is very large, plain and persistent reverberation pattern occur. An illustration of the
384 relationship between void spreads and radar footprint is shown in Figure 4. It suggests the
385 appearance of void in B-scan depends on not its physical spread but also the radar footprint which
386 is controlled by three factors: (1) void depth; (2) antenna frequency and (3) wave velocity.

387
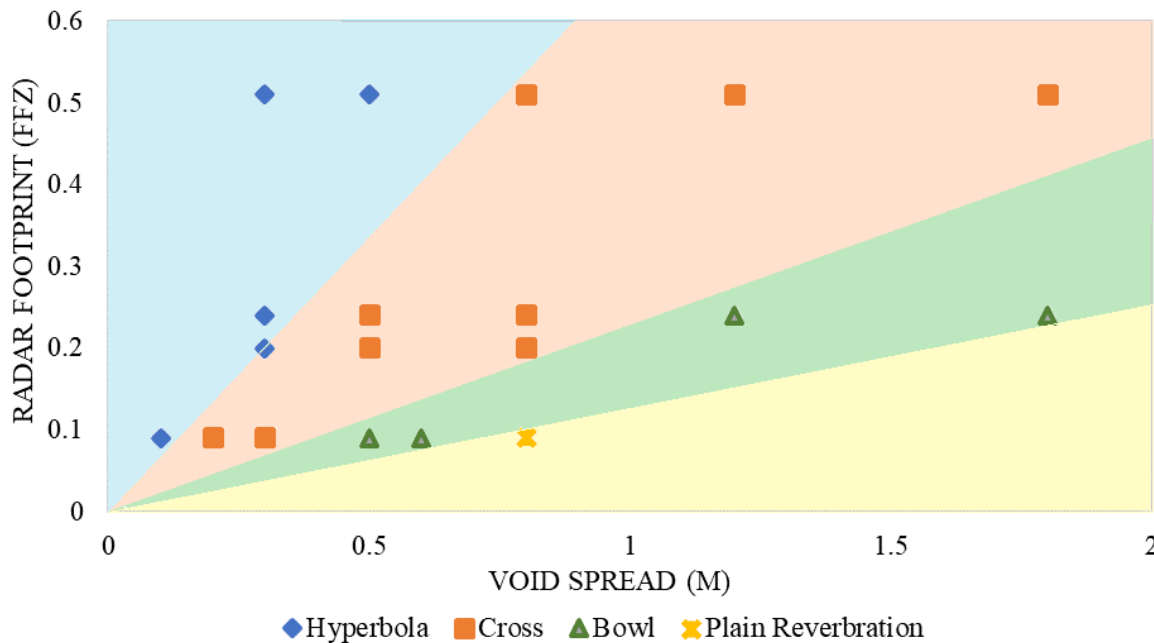
388   Figure 4 A summary of simulations on the relationship between void spreads and radar footprint

389   2) The road structure influences the GPR reflections of voids

390 Both site experiment and FDTD simulations illustrated that the mesh rebar in the concrete pave
391 road distorted the GPR reflections severely. The shape of GPR reflections of voids was broken by
392 the reflection of the mesh rebar. The typical patterns, like hyperbola, cross, bowl and plain
393 reverberation in rebar-free environment as in bituomous road, were hardly distinguishable. It is
394 because the GPR wave could not penetrate the metallic rebars, yielding a non-void reverberation
395 ringing between the antenna and rebars. Thus the voids were presented as the discontinuous yet
396 heavy reverberation in the B-scans of the concrete road. In contrast, the reverberation did not exist
397 in the bituminous road because of absence of rebars. Besides, the different road layers did not
398 manifest a significant impact on the GPR reflections as the dielectric properties of each road layers
399 were similar as predicted by the CRIM calculation.

4.2 Two limitations

1) Heavy scattering in the subsurface

Discrepancies are inevitable between experiments and simulations, as shown in Table 3 of the Shek Mun experiment. In practice, the underground environment could be much more complicated. Mie scattering caused by unexpected targets with size comparable to GPR wavelength is often observed in real practices. On the other hand, the simulation models are assumed to be relatively homogeneous. In the roads surveys, there are many underground utilities buried underneath, which also generate GPR responses and distort the response of air voids. Without convincing real data with ground truth results, it is difficult to prove the validatity or practical applications of these simulations with confidence. Yet, they form an indispensable basis for building forward models in more complicated scenarios, and then pattern recognition for decision-making of void or no-void during any void survey..

2) Geometry of voids and source of excitation

Firstly for geometry of voids, the shape and geometry are hardly known. In this study, only regular shape, or more explicitly the spheres and rectangles of voids (with surface roughness of the void-soil interface) were considered for the sake of computation efficiency and simplicity. Secondly for source of wave excitation, the energy in FDTD was excited from a point source, while in reality, the GPR signal was emitted from the antenna (with certain width) following equation [1].

Conclusion

Through carefully designed empirical experiments and FDTD numerical simulations, the study quantitatively investigates the GPR responses of underground air void with various sizes. Air voids in a relatively homogenous laboratory were used to observe the GPR response and compared with GPR response that is free from scattering. It was found that along with the different ratios of void spread to radar footprint; different patterns would present, and these patterns can be applied as fingerprints for air void identification. A site experiment was conducted to investigate the effect of the road structure on the GPR response of voids. It was found that GPR responses of voids under road structures were highly distorted by the rebars. And air voids under reinforcements present with stronger reverberation. Then two types of road structures: bituminous road and a concrete road were modelled to observe the impacts of void geometry to the GPR signals. In general, the GPR responses can be categorized into four patterns: hyperbola, cross, bowl, and plain reverberation. With knowledge of the GPR response of air voids, the efficiency of void identification can be improved, and the void with its size can be depicted from the GPR data.

Generally speaking, through categorizing the GPR responses of subsurface voids, a fingerprint database of the void patterns can be established. These typical patterns can serve as a guideline for operators to detect the invisible and shallow subsurface voids. Through recognizing localized anomalies through C-scans, voids can be roughly located and suspected for pattern recognition built based on forward modelling. In this way, preliminary judgments on the void existence and void size can be defined from the GPR data. An attempt of such effort has been reported in Luo & Lai (2020), which utilized the typical patterns to locate and depicts voids from GPR data. It relieved the effects of scattering by adjusting the sensitivity of the pattern recognition algorithm. However, to improve the precision and accuracy of the void identification with automatic

441 techniques, a more robust training set is required. A robust training set demands sufficient and
442 comprehensive data is always required and the development is in a very preliminary stage.

443

444 Reference

445 Annan, A., & Cosway, S. (1992). Simplified GPR beam model for survey design *SEG Technical*
446   *Program Expanded Abstracts 1992* (pp. 356-359): Society of Exploration Geophysicists.
447 Annan, A. P. (2004). Ground Penetrating Radar Applications, Principles, Procedures. Mississauga,
448   Canada: Sensors and Software.
449 ASTM D6432 (2011) Standard Guide for Using the Surface Ground Penetrating Radar Method for
450   Subsurface Investigation
451 Casas, A., Lazaro, R., Vilas, M., & Busquet, E. (1996). Detecting karstic cavities with ground
452   penetrating radar at different geological environments in Spain. Paper presented at the
453   Proceedings of the 6th International Conference of Ground Penetrating Radar.
454 Chan, C. Y., & Knight, R. J. (2001). Laboratory measurements of electromagnetic wave velocity in
455   layered sands. Water resources research, 37(4), 1099-1105.
456 Courant, R., Friedrichs, K., & Lewy, H. (1928). Über die partiellen Differenzengleichungen der
457   mathematischen Physik. Mathematische annalen, 100(1), 32-74.
458 Cullity, B. D., & Graham, C. D. (2008). Introduction to Magnetic Materials (Vol. 2).
459 Davidson, D. B. (2010). Computational electromagnetics for RF and microwave engineering:
460   Cambridge University Press.
461 Farley, M., Water, S., Supply, W., Council, S. C., & Organization, W. H. (2001). Leakage
462   management and control: a best practice training manual.
463 Giannopoulos, A. (2005). Modelling ground penetrating radar by GprMax. Construction and
464   Building Materials, 19(10), 755-762.
465 Goodman, D., & Piro, S. (2013). GPR remote sensing in Archaeology (Vol. 9). New York: Springer.
466 Hastings, F. D., Schneider, J. B., & Broschat, S. L. (1995). A Monte-Carlo FDTD technique for rough
467   surface scattering. IEEE transactions on antennas and propagation, 43(11), 1183-1191.
468 Hastings, F. D., Schneider, J. B., & Broschat, S. L. (1996). Application of the perfectly matched
469   layer (PML) absorbing boundary condition to elastic wave propagation. The Journal of the
470   Acoustical Society of America, 100(5), 3061-3069.
471 HyD. (2017a). Typical Bituminous Pavement Construction. Retrieved from
472   https://www.hyd.gov.hk/en/publications_and_publicity/publications/technical_docume
473   nt/hyd_standard_drawings/doc/section_1/pdf/H1101C.pdf
474 HyD. (2017b). Typical Concrete Pavement Construction. Retrieved from
475   https://www.hyd.gov.hk/en/publications_and_publicity/publications/technical_docume
476   nt/hyd_standard_drawings/doc/section_1/pdf/H1102B.pdf
477 Jol, H. M. (2009). Ground Penetrating Radar Theory and Applications: Oxford: Elsevier.
478 Kofman, L., Ronen, A., & Frydman, S. (2006). Detection of model voids by identifying
479   reverberation phenomena in GPR records. Journal of Applied Geophysics, 59(4), 284-299.
480 Lai, W., Tsang, W., Fang, H., & Xiao, D. (2006). Experimental determination of bulk dielectric
481   properties and porosity of porous asphalt and soils using GPR and a cyclic moisture
482   variation technique. Geophysics, 71(4), K93-K102.

483   Lai, W. W., Chang, R. K., & Sham, J. F. (2017). Detection and imaging of city's underground void
484   by GPR. Paper presented at the Advanced Ground Penetrating Radar (IWAGPR), 2017 9th
485   International Workshop on.
486   Lai, W. W., Chang, R. K., & Sham, J. F. (2018). A blind test of nondestructive underground void
487   detection by ground penetrating radar (GPR). Journal of Applied Geophysics, 149, 10-17.
488   Lai, W. W. L., Chang, R. K. W., Sham, J. F. C., & Pang, K. (2016). Perturbation mapping of water
489   leak in buried water pipes via laboratory validation experiments with high-frequency
490   ground penetrating radar (GPR). Tunnelling and Underground Space Technology, 52, 157-
491   167. doi:10.1016/j.tust.2015.10.017
492   Luo, T. X., Lai, W. W., Chang, R. K., & Goodman, D. (2019). GPR imaging criteria. Journal of Applied
493   Geophysics, 165, 37-48.
494   Luo, T. X. H., & Lai, W. L. (2020). GPR pattern recognition of shallow subsurface air voids.
495   Tunnelling and Underground Space Technology, In press.
496   NDT.net. (2011). Determination of dielectric properties of insitu concrete at radar frequencies.
497   Retrieved from https://www.ndt.net/index.php
498   Schneider, J. B. (2010). Understanding the Finite-Difference Time-Domain Method.
499   UUS-SPEC (2019) Specification for Non-destructive testing, surveying, imaging ad diagnosis for
500   Underground Utilities 1,2 Ground Penetrating Radar. UUS-SPEC
501   Warren, C., Giannopoulos, A., & Giannakis, I. (2016). gprMax: Open source software to simulate
502   electromagnetic wave propagation for Ground Penetrating Radar. Computer Physics
503   Communications, 209, 163-170.
504   Wu, H. Y. (2015). Characterization of Shallow Subsurface Air-filled Voids by Ground Penetrating
505   Radar. (Bachelor of Science), The Hong Kong Polytechnic University, Hong Kong.
506   Xu, X., Zeng, Q., Li, D., Wu, J., Wu, X., & Shen, J. (2010). GPR detection of several common
507   subsurface voids inside dikes and dams. Engineering Geology, 111(1-4), 31-42.
508   doi:10.1016/j.enggeo.2009.12.001
509   Yee, K. (1966). Numerical solution of initial boundary value problems involving Maxwell's
510   equations in isotropic media. IEEE transactions on antennas and propagation, 14(3), 302-
511   307.

512